# In situ spectroscopic ellipsometry and rigorous coupled wave analysis for real time profile evolution of atomic layer deposited films inside SiO<sub>2</sub> nanotrenches ©

Cite as: J. Vac. Sci. Technol. A **40**, 062403 (2022); https://doi.org/10.1116/6.0001937 Submitted: 27 April 2022 • Accepted: 26 August 2022 • Published Online: 30 September 2022

🗓 S. Novia Berriel, Corbin Feit, Nick Keller, et al.

## COLLECTIONS

Note: This paper is part of the 2023 Special Topic Collection on Atomic Layer Deposition (ALD).



This paper was selected as an Editor's Pick















# 

Cite as: J. Vac. Sci. Technol. A **40**, 062403 (2022); doi: 10.1116/6.0001937 Submitted: 27 April 2022 · Accepted: 26 August 2022 · Published Online: 30 September 2022







S. Novia Berriel, <sup>1</sup> D Corbin Feit, <sup>1</sup> Nick Keller, <sup>2</sup> Nicholas G. Rudawski, <sup>3</sup> and Parag Banerjee <sup>1,4,5,6,a)</sup> D

### **AFFILIATIONS**

- Department of Materials Science and Engineering, University of Central Florida, Orlando, Florida 32816
- <sup>2</sup>Onto Innovation Inc., Wilmington, Massachusetts 01887
- Research Service Centers, University of Florida, Gainesville, Florida 32611
- <sup>4</sup>Nano Science and Technology Center, University of Central Florida, Orlando, Florida 32816
- <sup>5</sup>Florida Solar Energy Center, University of Central Florida, Orlando, Florida 32816
- <sup>6</sup>REACT faculty cluster, University of Central Florida, Orlando, Florida 32816

Note: This paper is part of the 2023 Special Topic Collection on Atomic Layer Deposition (ALD).

<sup>a)</sup>Author to whom correspondence should be addressed: parag.banerjee@ucf.edu

### **ABSTRACT**

Rigorous coupled wave analysis (RCWA) is conducted on  $in\ situ$  spectroscopic ellipsometry data to understand profile evolution during film deposition inside nanotrenches. Lithographically patterned SiO<sub>2</sub> nanotrenches are used as test structures. The nanotrenches are 170 nm wide at the top with a taper angle of 4.5° and are 300 nm in depth. Atomic layer deposition of ZnO is used as a model process where the thickness (cycles) of the film is varied from 0 (0 cycles) to 46 nm (300 cycles). The analysis predicts transient behavior in deposition affecting film conformality and changes to the trench taper angle. In the process, the aspect ratio varies from 2.05 at the start of the process to 6.67 at the end. The model predicts changes in the refractive index of the ZnO film as a function of thickness. The real and imaginary parts of the refractive index at a wavelength of 350 nm change from 1.81 to 2.37 and 0.25 to 0.87, respectively. Scanning electron microscopy cross sections confirm thickness at the top and bottom of the trench to within 13% of those predicted by RCWA. The experimentally measured conformality degrades as film deposition proceeds from 97.3% at 100 cycles to 91.1% at 300 cycles. These results demonstrate the potential of using RCWA for continuous and  $in\ situ$  monitoring of growth inside 3D nanostructures.

Published under an exclusive license by the AVS. https://doi.org/10.1116/6.0001937

### I. INTRODUCTION

Atomic layer deposition (ALD) is a method to deposit highly conformal thin films using a sequential set of two or more self-limiting surface reactions. These reactions are repeated cyclically to achieve near monolayer fidelity in film growth. The self-limiting nature of the surface reactions allows for the deposition of highly conformal ALD films inside high aspect ratio (AR) structures. This defining characteristic of ALD has been exploited to develop 3D nanostructured devices such as DRAM

cell capacitors, electrostatic supercapacitors, battery electrodes, and solar cells.

One of the challenges of depositing ALD films inside high AR nanostructures is to optimize the process for high conformality. Deposition in high AR nanostructures can become transport or diffusion limited, causing less conformal films to be deposited. <sup>10,11</sup> Further, for multicomponent/nanolaminate structures, the composition of the film stack can alter from the top of the trench to the bottom. <sup>12</sup> The conformality of the films is an important factor for device scalability and reliability and can be difficult to determine in

trenches and other nonplanar substrates. Currently, ex situ measurements, such as electron microscopy coupled with elemental analysis techniques (such as energy dispersive x-ray spectroscopy), can be used to characterize ALD film uniformity on nonplanar substrates. 13 Specialized structures like PillarHall substrates help to quantify conformality of various processes. 10,14,15 However, there are no techniques that can monitor film deposition inside 3D nanostructures in real time.

In situ spectroscopic ellipsometry (SE) is a powerful characterization tool that has been extensively used to study the growth of ALD films in real time on planar substrates. 16-18 SE captures the change in polarization of incident light to determine the thickness and optical constants of the film being deposited. This is not, however, the only use of SE. For example, studies such as that of Hilfiker et al. have used SE to determine the dielectric function of materials. 19,20 Pal et al. and Spencer et al. use SE to study optical bandgap and electronic band structure. 21,22 Film roughness has also been studied.<sup>23,24</sup> Kilic et al. used in situ SE to monitor evolution of surface roughness and individual layer thickness in an ALD process.<sup>25</sup> Real-time acquisition of the SE data allows one to determine film thickness and optical constants over time, and, thus, growth rates and dynamic changes to optical properties of the film can be obtained, improving understanding of deposition processes. The key to effectively use SE is to integrate the data acquired with a physics-based optical model that can accurately describe the polarization response of the film/substrate combination. SE, however, fails when it comes to nonplanar substrates with complex nano topologies.

Alternately, modeling of deposition inside 3D nanostructures is a valuable approach to predict conformality of ALD processes. Models are constructed by recognizing that precursor access to surfaces inside 3D nanostructures is diffusion controlled. 11 Many analytical models have been developed for describing ALD in holes of various aspect ratios.<sup>26-28</sup> Trenches have also been modeled via Monte Carlo or Ballistic computation. 5,29 Fewer analytical models exist for trenches, such as Ylilammi et al. 10 and Yim et al., 11 modeling diffusion in lateral trenches, and Fadeev and Rudenko<sup>30</sup> studying flux of particles at the walls of angled trenches as a function of wall angle. However, these models have not been coupled to in situ techniques such that they cannot give insight into real-time profile evolution inside 3D structures.

To overcome the difficulties of optically modeling patterned structures, the rigorous coupled wave analysis (RCWA) method has been used. 31-33 The RCWA method is a frequency domain method that makes use of Fourier harmonics to describe 2D periodic structures. In principle, SE data captured in situ can be modeled with the RCWA method to determine the growth rate of the film over time on a patterned substrate, as well as determine conformality in real time.

Here, we show the evolution of topology as an ALD ZnO film is deposited inside a periodic nanotrench pattern, as modeled by the RCWA method. The model predicts film thickness, AR, and conformality changes in real time within the trenches as a function of the deposition time. Comparison of the predicted film thickness with scanning electron microscope (SEM) cross-sectional images, which are "snapshots" in time, shows the values to be within 13% of each other. These results highlight the suitability of using SE coupled to RCWA for the study of film deposition inside 3D nanostructured substrates.

### II. EXPERIMENTAL DETAILS

Patterned SiO<sub>2</sub> trench coupons of dimensions 25.4 × 25.4 mm<sup>2</sup> were obtained from Onto Innovation and diced by Grinding and Dicing Services Inc<sup>®</sup>. The coupons consisted of trenches of SiO<sub>2</sub> on Si. A blanket SiO<sub>2</sub> film was first lithographically patterned and subsequently dry etched to produce parallel lines, much like a diffraction grating. The cross-sectional schematic of a trench is shown in Fig. 1(a) and consisted of an opening of 170 nm at the top of the structure and results in a "chamfer." The trench narrowed to form a tapered sidewall with a reduced opening of 122 nm and a gap at the bottom of 82 nm (also known as, base critical dimension). The entire structure was 300 nm high and the sidewall was 250 nm high. The sidewall made an angle,  $\theta \sim 85.5^{\circ}$  with respect to the horizontal. Thus, the taper angle ( $\alpha$ ) is defined as 90-84.5 = 4.5°. Further, we define the AR of the trench consisting of the tapered sidewall as sidewall length (L)/opening width (W) 250/122 = 2.05. We note here that the AR for this structure is not high compared to many reported in the literature but serves as a platform for the demonstration of 3D topography evolution monitored using in situ ellipsometry.

ALD ZnO was deposited using a Fiji Gen2 ALD System from Veeco®. The ZnO film as deposited was crystalline and in the wurtzite structure as confirmed previously.<sup>38</sup> The process consisted of alternate pulses of diethyl zinc (DEZ, Sigma Aldrich, CAS:557-20-0  $\geq$  52 wt. % in hexane) at 60 ms and de-ionized water (H<sub>2</sub>O) at 60 ms. The bubblers were kept at room temperature. The purge time used between pulses was 10 s. On a planar substrate, this recipe gives a growth rate of 0.17 nm/cy with a refractive index (n) of 1.9 as measured at 633 nm. A total of 300 cycles were conducted to grow the ZnO film which took approximately 90 min. The temperature of deposition was 200 °C. A base pressure of the chamber was maintained at 16.67 Pa, whereas the peak pressure during pulsing was recorded as 27.33 Pa for DEZ and 26.00 Pa for H<sub>2</sub>O. SE was used to track the film growth on the patterned substrate.

An FEI Helios Nanolab 600i dual focused ion beam (FIB)/ scanning electron microscope (SEM) was used to prepare and image cross sections of the trenches. Prior to preparation and imaging, the trenches were ex situ coated with permanent marker to fill in the gaps between trenches to minimize curtaining effects during subsequent FIB milling<sup>39</sup> and then ex situ evaporation coated with ~75 nm of carbon. Preparation of the cross-sectional faces began with in situ 2 kV, 2.7 nA SEM- and subsequent 30 kV, 50 pA FIB-assisted Pt deposition to produce a  $\sim 1 \,\mu m$  thick protective strap. Next, a trench was milled above the Pt strap using a 30 kV, 5.0 nA FIB setting with the regular cross-sectional pattern and 5° of over-tilt to produce the initial cross-sectional face. The final cross-sectional face was produced by subsequent milling with 30 kV, 1.0 and 0.3 nA FIB settings using the cleaning crosssectional pattern and 2.5° and 0° of over-tilt, respectively. High-resolution SEM imaging of the cross-sectional faces was performed at 2 kV, 11 pA using immersion mode with a positively biased through-lens detector (secondary + backscattered mode) at a

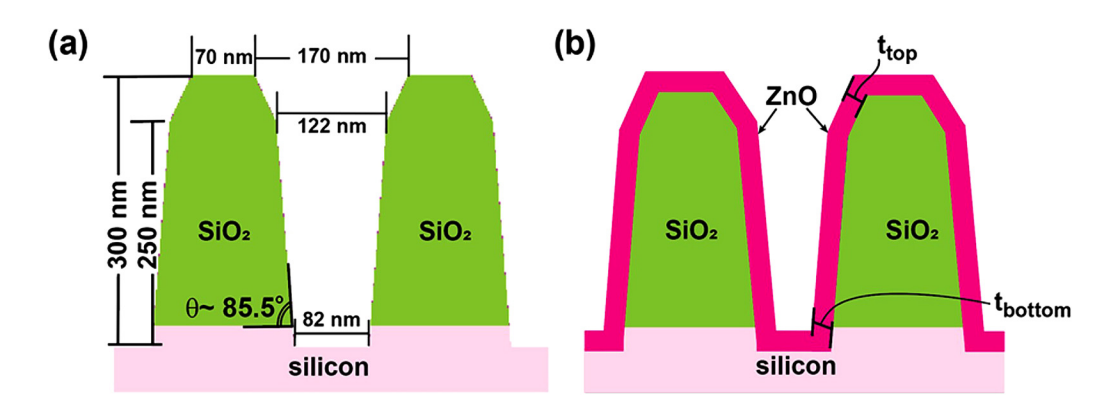


**FIG. 1.** (a) Cross section of  $SiO_2$  trench showing dimensions of the structure. The pitch is 240 nm. The total height is 300 nm, and the height of the angled sidewall is 250 nm. Given the trench opening is 122 nm, the A.R. is 2.05. (b) Schematic of the ZnO film deposited inside the trench shows the thickness modeled at the top and bottom using RCWA.

4 mm working distance. The stage tilt was set to 52° during imaging resulting in the cross-sectional faces being tilted 38° relative to the SEM beam. Dynamic focus was used to compensate for tilt of the cross-sectional face relative to the SEM beam and all SEM images were tilt corrected. ImageJ® was used to analyze all SEM images.

The film growth was tracked *in situ* using an M-2000 spectroscopic ellipsometer (SE) from J. A. Woollam<sup>®</sup>. The ellipsometer light source and detector were attached to a FIJI<sup>®</sup> Gen2 ALD system using specialized mounts on 69.85 mm conflat flanges with quartz windows. The windows are internally purged with 50 SCCM of argon gas. The angle of incidence and reflection of the light was  $69.5^{\circ}$ . The ellipsometer acquired data for wavelengths from 271 to 1688 nm in time intervals of  $\sim 3$  s.

The SE data were modeled using the NanoDiffract optical critical dimension software from Onto Innovation. A model was constructed to measure ZnO conformality over the deposition time. The base model of the grating, including SiO<sub>2</sub> base critical dimension, Si over-etch,  $\alpha$ , and SiO $_2$  height was constructed for process time, t = 0 and then fixed. The ZnO film was modeled as a spacer to cover the side wall, a fill to cover the bottom of the grating, and a top layer to cover the top of the grating. The locations of the top thickness  $(t_{top})$  and bottom thickness  $(t_{bottom})$  are shown in Fig. 1(b). The bottom fill is coupled to the bottom sidewall thickness, and the top layer is coupled to the top sidewall thickness to prevent discontinuity in the film structure. Conformality is defined as  $(100 \times t_{bottom}/t_{top})$ %. The ZnO film was defined by two Tauc-Lorentz oscillators with the amplitudes left floating.<sup>40</sup> Optical constants were also left floating for the purposes of this model.

### **III. RESULTS AND DISCUSSION**

Representative snapshots of *in situ* ellipsometry data—i.e., changes to polarization intensity ( $\Psi$ ) and phase ( $\Delta$ ), collected at time t=0—are shown in Figs. 2(a) and 2(b) for planar Si and SiO<sub>2</sub> trench wafers, respectively. We note that the ( $\Psi$ ,  $\Delta$ ) curves shown

in Fig. 2(b) are for the case where the plane of incidence is oriented perpendicular to the trench, though results from the parallel orientation (not reported here) yield similar results. This is because the modeling software is able to account for azimuth angle as a parameter and compensate for any changes due to different azimuth angles. Compared to the Si wafer, the  $(\Psi, \Delta)$  curves obtained for the SiO<sub>2</sub> trench pattern are markedly different due to a combination of (1) differences between the optical properties of Si and SiO<sub>2</sub> and (2) the periodic features of the trench. Using effective medium approximation (EMA)<sup>41</sup> and modeling the trench as a homogeneous mixture of SiO<sub>2</sub> + air (49% by volume), the effective thickness of the SiO<sub>2</sub> trench can be modeled as  $281.4 \pm 1.7$  nm (details in the supplementary material)<sup>47</sup> which is close to the true height of the structure shown in Fig. 1. However, information on

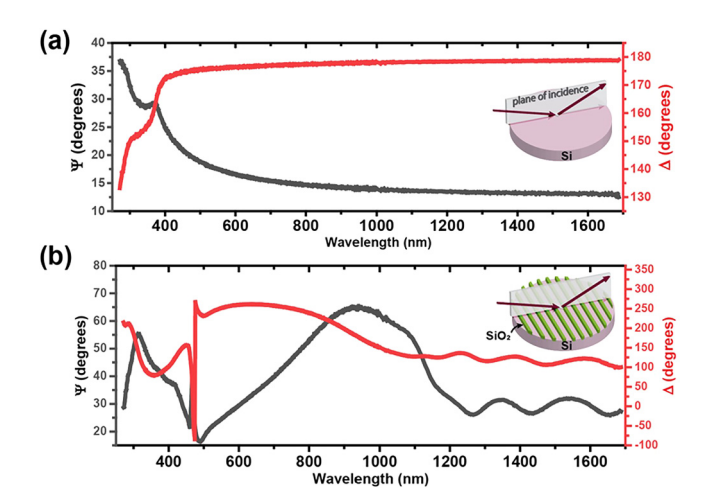


**FIG. 2.** (a) Polarization data  $(\psi, \Delta)$  as obtained on a planar Si substrate and (b) on a substrate with SiO<sub>2</sub> trench structures where the incident beam is perpendicular to the grating pattern.



topological features of the trench cannot be gleaned from this approach. Thus, the EMA model yields limited information related to the 3D structure and dimensions of the trench. Further, during deposition, real-time changes to the trench structure, film thickness at the top and bottom of the trench, AR and conformality of the process cannot be obtained.

In contrast to the traditional SE approach, the RCWA approach generates real-time topology data of the deposited film inside 3D nanotrenches. ONTO's NanoDiffract® software is able to accomplish this directly from the above  $(\Psi, \Delta)$  curves. The Mueller matrix components<sup>42</sup> and the fitting of these data as a function of time are provided in the supplementary material.<sup>47</sup> The resulting output is shown in Fig. 3(a) with the modeled film thickness at the top  $(t_{top})$  and bottom  $(t_{bottom})$  of the trench given as a function of ALD cycles.

Based on Fig. 3(a), we divide the deposition into three observable stages. In stage I (i.e., 0-125 ALD cycles), the process appears to be highly conformal with no observable difference between  $t_{top}$ and  $t_{bottom}$ . This is not surprising, since the AR of the given structure is not high. In stage II (i.e., 125-225 ALD cycles), beginning at 50 min (i.e.,  $t_{top} \sim 22$  nm),  $t_{bottom}$  deviates with conformality dropping to 79%. Subsequently,  $t_{bottom}$  recovers with a faster growth rate compared to  $t_{top}$  until at the end of stage II,  $t_{top}$  and  $t_{bottom}$  thicknesses are nearly the same again. In stage III (i.e., 225-300 ALD cycles),  $t_{top}$  and  $t_{bottom}$  are nearly equal. This point of convergence for  $t_{top}$  and  $t_{bottom}$  is labeled as "critical thickness,"  $t_{crit} = 46 \text{ nm}$ . The trends observed and the importance of  $t_{crit}$  will be described in the geometrical modeling section. At the end of 300 cycles of ALD, the  $t_{top}$  and  $t_{bottom}$  are both predicted to be ~48 nm. Thus, RCWA provides a real-time description of the changes to 3D topology during deposition inside the nanotrenches.

Because of the dynamic changes recorded to  $t_{top}$  and  $t_{bottom}$ , the taper angle and AR can be modeled. In Fig. 3(b), the taper angle  $\alpha$  is shown as a function of ALD cycles. As expected,  $\alpha$  begins at 4.5° at the start of deposition. However,  $\alpha$  appears to

oscillate, increasing to 5.2° at the end of stage I, then dropping to 2.7° at the end of stage II before recovering to 4.8° at the end of deposition. We note that from an experimental verification point of view, such minute changes to taper angle can be difficult to measure and, therefore, verify. Nonetheless, the oscillation in  $\alpha$  can provide insights into the deposition process when compared with previously published model predictions. Figure 3(c) shows the extracted AR due to deposition. Based on the  $t_{top}$  and  $t_{bottom}$ , the time-dependent AR is given by  $AR = \frac{L - t_{bottom}}{W - 2 \times t_{top}}$ . The AR of the structure increases as deposition proceeds varying from 2.05 at the start to 6.67 at the end of the deposition (i.e., 300 cycles) of the ALD ZnO inside the trench.

The estimated refractive index (n) and extinction coefficient (k), determined at 350 nm, of ALD ZnO are shown in Fig. 3(d). A wavelength of 350 nm is used, as the extinction coefficient is nonzero at this wavelength (i.e., finite absorbance) and drops off to zero for photon energies less than the band gap of ZnO (i.e., wavelength >  $\sim 360$  nm). Both n and k are considered as location independent constants for the purpose of RCWA, but are time dependent, i.e., n and k vary during deposition. The estimated n starts low ( $\sim 1.81$ ) at low thickness and then steadily increases to a final value of 2.37, in line with reported values in the literature. The low value of n at the beginning of the deposition could be related to the island-like nucleation that is often observed during ALD ZnO on dielectric surfaces. The k varies from 0.25 to 0.87, which is close to reported values.

To verify model predictions, cross-sectional SEM images were obtained for ALD processes at 0, 100, 200, and 300 cycles. Thickness comparison results of this analysis are shown in Fig. 4(a). At 100 cycles, while the model predicts a  $t_{top}$  of 16.5 nm, we find that  $t_{top}$  observed is  $15.0 \pm 1.4$  nm. Similarly,  $t_{bottom}$  at 100 cycles from the model is 18.2 nm, and from SEM cross sections is  $14.6 \pm 1.1$  nm (experimental conformality 97.3%). At 200 cycles, the  $t_{top}$  predicted from the model is 35.6 nm, whereas the thickness measured is  $28.8 \pm 3.0$  nm. The  $t_{bottom}$  predicted from the model is

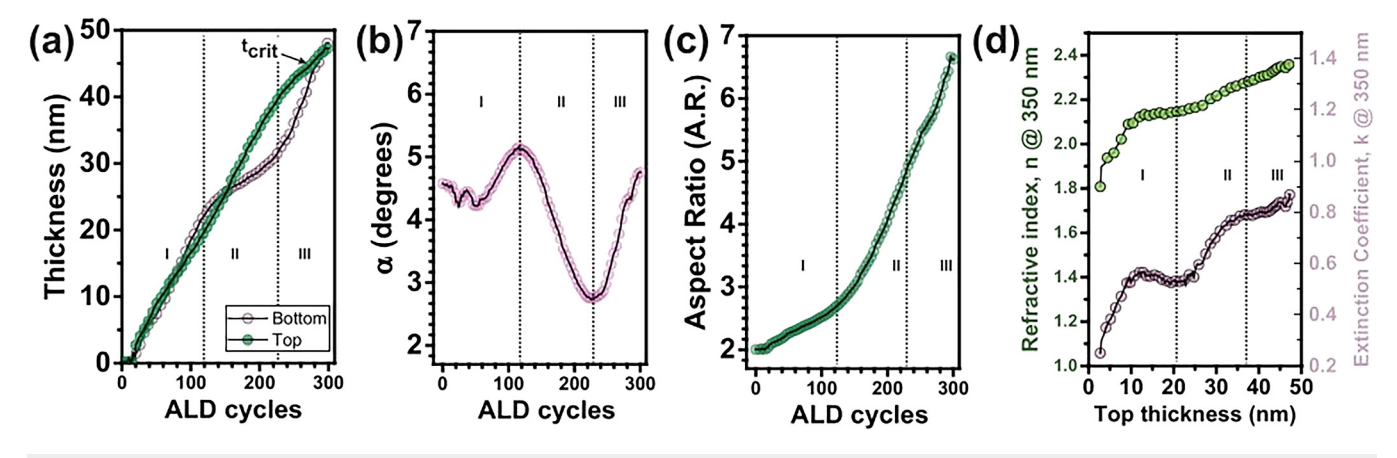


FIG. 3. (a) Thickness at top and bottom of the trench as a function of ALD cycles. (b) The taper angle "α" as a function of ALD cycles. (c) The A.R. varies from 2.05 to 6.67 as deposition proceeds. (d) Refractive index "n" (left axis) and extinction coefficient "k" (right axis) at 350 nm as a function of top thickness. Symbols indicate model data points, solid lines serve as mere guide for the eye, and dashed lines demarcate stages of deposition.

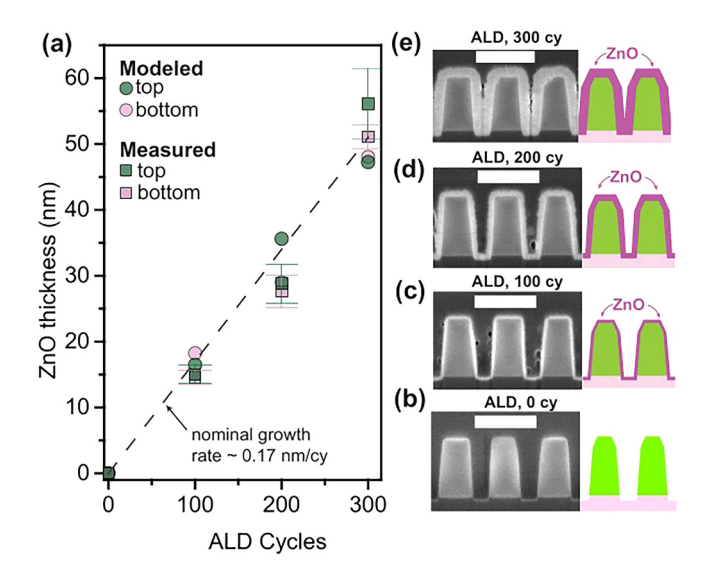


FIG. 4. (a) ALD ZnO thickness as a function of ALD cycles. Data are compiled from the model for top and bottom and compared to the measured top and bottom thickness from SEM cross sections. The error bars represent the standard deviation of eight individual measurements in the SEM cross sections. The dotted line represents the nominal growth rate of 0.17 nm/cycle on a planar susbtrate. (b)–(e) SEM cross sections and corresponding model cross sections from RCWA are shown for 0, 100, 200, and 300 ALD cycles. Scale bar in (b)–(e) represents 300 nm.

29.0 nm and from SEM cross sections is  $27.6 \pm 2.5$  nm (experimental conformality 95.8%). Lastly, at 300 cycles, the  $t_{top}$  from the model is 47.3 nm, whereas the thickness observed is  $56.1 \pm 5.4$  nm (experimental conformality 91.1%). Since the sidewalls have merged at the bottom, we report  $t_{bottom}$  measured at the top of the seam formed. The model  $t_{bottom}$  is 48.1 nm and from SEM cross sections is  $51.1 \pm 1.8$  nm. Overall, the film thickness from RCWA and SEM cross sections are within an average of 13% of each other. The seam height from the model is 91 nm and the average seam height measured inside ten trenches is  $173.3 \pm 18$  nm.

In Fig. 4(b), SEM cross section and model cross section are shown for the undeposited (i.e., 0 cycle) trench. While the dimensions of the SiO<sub>2</sub> trench match well, the chamfer is not obvious in the cross-sectional SEM. This difference in cross-sectional profiles could yield differences between measured and predicted thickness as indicated in the above paragraph. In Figs. 4(c)-4(e), 100, 200, and 300 cycle cross-sectional SEM images and model cross sections are shown, respectively. The visual similarity between SEM and model cross sections is evident.

We seek to explain the above results by understanding the interaction of the various growth fronts inside the  $SiO_2$  trench. By advancing the ALD growth fronts in a direction normal to the deposition surface, changes to the trench structure can be visualized. The advancing growth front at the bottom of the trench is used to determine the "pinch-off" region when the three surfaces, i.e., the bottom and two sidewalls, merge. The thickness at pinch-off is defined as  $t_{crit}$ . The concept is shown schematically in Fig. 5(a).

The pinch-off point "O" is equidistant from the projection of the three surfaces RD, DE, and ES on a 2D plane. The three surfaces form tangents to the circle shown with center at O and radius,  $t_{crit}$ .

From triangle STE, we get

$$\tan \alpha = \text{ET/TS} = (W_t - W_b)/2.h,\tag{1}$$

where  $W_t$  and  $W_b$  are the width of the trench at the top and bottom, respectively, and h is the height. From triangle OPB, we get

$$\sin \alpha = \text{OB/OP} = t_{crit}/(t_{crit} + x),$$
 (2)

where x is the distance inside the Si substrate where the tangents meet. Finally, from triangle AEP,

$$\tan \alpha = AE/AP = W_b/2x. \tag{3}$$

Thus, the three unknowns,  $t_{crit}$ , x, and  $\alpha$  can be numerically solved using the above three equations.

In Fig. 5(b), we show the schematic of the growth fronts as individual layers. At the point of convergence "O," the bottom front ceases to exist and growth proceeds via deposition on the sidewalls only. In Fig. 5(c), the variation of  $t_{crit}$  is shown as a function of various top (Y axis) and bottom (X axis) gaps. For the current case, a top gap of 122 nm and a bottom gap of 82 nm yield a  $t_{crit}$  of 44 nm. When compared to Fig. 3(a),  $t_{crit}$  obtained via RCWA (i.e., 46 nm) is reasonably close to the value obtained via geometrical modeling.

During stage I (0-125 cycles), when the thickness is low and the AR is not significantly impacted, the ALD process is highly conformal as determined by RCWA (>95%) and by SEM cross sections (97.3%). In stage II (125-225 cycles), the RCWA model predicts  $t_{bottom}$  to first decrease and a loss in conformality to 79% is observed. However, according to the SEM cross section in Fig. 4(d) at 200 cycles, the deposition maintains a conformality of 95.8%. This discrepancy in conformality could be related to the absence of a chamfer, as indicated by cross-sectional SEM images of the undeposited nanotrench structure. In stage III (225-300 cycles), additional deposition causes the growth rate of  $t_{bottom}$  to recover. The RCWA predicts >100% conformality while SEM cross sections show the conformality to be 91.1%. Thus, while SEM cross sections are discretized snapshots in time, RCWA provides a quasicontinuous and temporal evolution of the 3D nanostructure as deposition proceeds. While differences in thickness predicted by RCWA and SEM cross sections exist, we note that these thicknesses are within an average of 13% of each other.

The idea of conformality >100% is counter intuitive but can be explained as an artifact of the RCWA approach. As stated before,  $t_{bottom}$  is coupled to the bottom sidewall thickness. Thus, as the three growth fronts in Fig. 5(b) merge, the bottom surface ceases to exist. Any growth along the vertical direction is determined by deposition on the sidewalls which make an angle  $\alpha$  with respect to the vertical axis. The increment in the film thickness along the vertical direction ( $\Delta t_{\perp}$ ) is given by  $\Delta t_{\perp} = t_{ALD}/\sin \alpha$  where,  $t_{ALD}$  is the growth rate/cycle for the ALD process on a planar surface. As previously noted, the RCWA constraints require

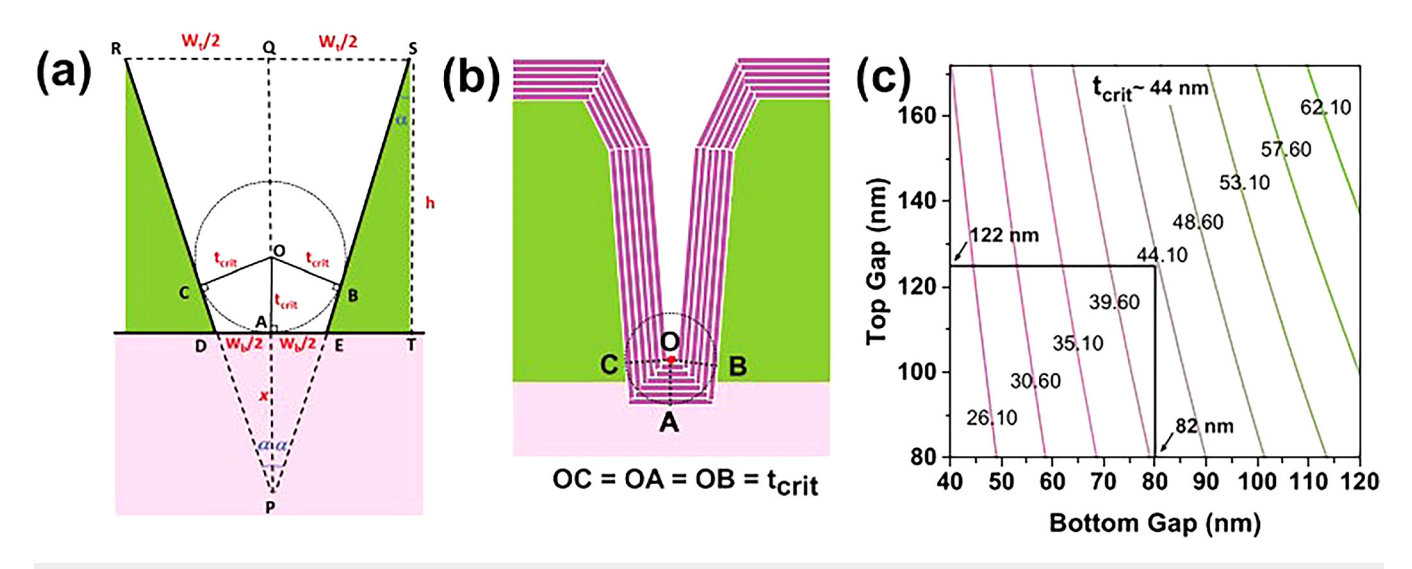


FIG. 5. (a) Geometrical model shows the point of convergence where the three growth fronts at the trench bottom meet at point "O" when the film thickness reaches t<sub>crit</sub>. (b) The point of convergence "O" is shown inside a trench as individual growth fronts merge. At point "O," the bottom front ceases to exist. (c) The t<sub>crit</sub> is plotted as a function of top and bottom gap of the trench. For the present study, the top and bottom width are 122 and 82 nm, respectively, and t<sub>crit</sub> is 44 nm.

that  $t_{bottom}$  be coupled to  $\Delta t_{\perp}$ , i.e., the growth rate along the vertical direction. This implies that  $t_{bottom}$  can see an *apparent* increase in the growth rate if the sidewalls are relatively close to each.

As a limiting case, consider the sidewall in the present trench structures, where  $t_{ALD}=0.17$  nm,  $\alpha=4.5^{\circ}$ , and, therefore,  $\Delta t_{\perp}=2.17$  nm. Such vertical growth rates are not realizable since  $t_{ALD}$  may not be 0.17 nm/cycle inside few nanometer wide openings left in the closing sidewalls. Nonetheless, RCWA model interprets increased  $t_{bottom}$  rates as  $\Delta t_{\perp}$  in the later part of stage II as the tapered sidewalls close the seam and can be considered an artifact of the modeling approach.

We now explain the oscillatory features in the time-dependent  $\alpha$  shown in Fig. 3(b). Fadeev and Rudenko<sup>30</sup> have modeled the effect of  $\alpha$  on changes to precursor flux approaching: (i) the trench sidewalls and (ii) the trench bottom, as a function of AR Small changes to  $\alpha$  (modeled for  $\pm 1^{\circ}$ ) affect the sidewall flux, fractional area coverage, and, therefore, film thickness, especially as AR increases. For the nanotrenches studied in this work,  $\alpha$  is 4.5° and, therefore, we expect these effects to be accentuated even though our AR is relatively low. We propose that the oscillations in  $\alpha$  point to dynamic changes to the taper angle where an initial  $\alpha$  of 4.5° causes a sufficient flux of precursors to reach the bottom region of the trench resulting in a near conformal film (stage I). As the AR increases, unreacted precursor molecules experience longer residence times at the bottom of the trenches. This leads to a thickness gain in  $t_{bottom}$  exceeding  $t_{top}$  and, therefore, an increase in  $\alpha$  (end of stage I). According to Fadeev and Rudenko<sup>30</sup> model, increase in  $\alpha$ leads to a lowering of the flux reaching the bottom of the trench, which in turn leads to a decrease of  $\alpha$ . This corresponds to stage II of the deposition profile and the oscillation perpetuates in time. Therefore, the temporal instability in  $\alpha$  could be a result of the interplay between  $\alpha$  and the precursor flux reaching the bottom of the nanotrench, given that these two parameters are inversely coupled to each other. The effect amplifies at higher AR The surprising aspect of the RCWA is that while the AR monotonically increases with thickness (i.e., as expected),  $\alpha$  shows the subtle oscillatory behavior otherwise not predicted by current models. The oscillation is expected to be observed until the sidewalls merge.

Optimizing ALD processes for demanding 3D nanostructures is challenging. Currently, ALD processes are run in the over-saturation limit to ensure high conformality of films. Process feedback on 3D nanostructures is obtained via *ex situ* techniques only. This makes process development inefficient. The availability of an *in situ* approach to monitor deposition inside periodic 3D nanostructures addresses this challenge. We note that our results have implications beyond monitoring ALD growth. Thus, plasma-enhanced ALD, chemical and physical vapor deposition techniques may benefit from this approach as well.

### **IV. CONCLUSIONS**

We have shown that *in situ* SE data modeled via RCWA can be used to obtain real-time dynamics of film growth inside periodic 3D nanotrenches. An ALD ZnO film was used as a model process to demonstrate this approach. Silicon substrates with patterned  $SiO_2$  nanotrenches, 250 nm deep and a taper resulting in a trench 122 nm wide at the top and 82 nm at the bottom, were used for deposition. The beginning AR was 2.05. As the deposition proceeded, RCWA tracked variations to ZnO thickness at the bottom and top of the trenches, conformality, AR, and the optical constants (n, k). The optical constants are in line with published values. The *in situ* data modeled using RCWA showed a transient loss of film conformality as the sidewall growth fronts approach each other, likely due to transport limited deposition. A more



subtle effect is seen in the sidewall taper angle, which appears to oscillate as deposition proceeds. The conformality is restored when the fronts of the sidewall begin to merge at the bottom of the trench at a film thickness of ~46 nm. A geometric model of the growth fronts at the bottom of the trench can explain the thickness variability over time. In contrast to the RCWA predictions of thickness, SEM cross sections obtained at three discrete time intervals showed film thickness to be within 13% of the predicted values. Film conformality appeared to monotonically decrease with increasing film thickness. The RCWA technique can provide *in situ* monitoring of growth behavior inside periodic 3D nanostructures, otherwise difficult to obtain via current *ex situ* techniques.

### **ACKNOWLEDGMENTS**

S.N.B. and P.B. acknowledge the funding from Semiconductor Research Corporation (SRC) under Grant No. 3026.001. C.F. and P.B. acknowledge support from the National Science Foundation (NSF) under Award No. 1908167. All authors acknowledge the Research Service Centers at the University of Florida for use of the FEI Helios Nanolab 600i dual FIB/SEM. The patterned wafers and the Nanodiffract software were kindly provided by ONTO.

### **AUTHOR DECLARATIONS**

### **Conflict of Interest**

The authors have no conflicts to disclose.

### **Author Contributions**

S. Novia Berriel: Data curation (equal); Formal analysis (equal); Investigation (equal); Writing – original draft (equal). Corbin Feit: Formal analysis (equal). Nick Keller: Formal analysis (equal); Investigation (equal); Software (equal). Nicholas G. Rudawski: Investigation (equal). Parag Banerjee: Conceptualization (equal); Methodology (equal); Project administration (equal); Supervision (equal); Writing – original draft (equal); Writing – review & editing (equal).

### **DATA AVAILABILITY**

The data that support the findings of this study are available from the corresponding author upon reasonable request.

### **REFERENCES**

- <sup>1</sup>S. M. George, Chem. Rev. 110, 111 (2010).
- <sup>2</sup>R. W. Johnson, A. Hultqvist, and S. F. Bent, Mater. Today 17, 236 (2014).
- <sup>3</sup>R. L. Puurunen, J. Appl. Phys. **97**, 121301 (2005).
- <sup>4</sup>M. Leskelä and M. Ritala, Angew. Chem. Int. Ed. 42, 5548 (2003).
- <sup>5</sup>H. C. M. Knoops, E. Langereis, M. C. M. Van De Sanden, and W. M. M. Kessels, J. Electrochem. Soc. 157, G241 (2010).
- <sup>6</sup>V. Cremers, R. L. Puurunen, and J. Dendooven, Appl. Phys. Rev. 6, 021302 (2019).
- <sup>7</sup>J. A. Kittl *et al.*, Microelectron. Eng. **86**, 1789 (2009).
- <sup>8</sup>P. Banerjee, I. Perez, L. Henn-Lecordier, S. B. Lee, and G. W. Rubloff, Nat. Nanotechnol. 4, 292 (2009).
- <sup>9</sup>X. Meng, X.-Q. Yang, and X. Sun, Adv. Mater. 24, 3589 (2012).
- <sup>10</sup>M. Ylilammi, O. M. E. Ylivaara, and R. L. Puurunen, J. Appl. Phys. 123, 205301 (2018).

- <sup>11</sup>J. Yim, E. Verkama, J. A. Velasco, K. Arts, and R. L. Puurunen, Phys. Chem. Chem. Phys. 24, 8645 (2022).
- <sup>12</sup>M. Coll and M. Napari, APL Mater. 7, 110901 (2019).
- <sup>13</sup>K. Arts, M. Utriainen, R. L. Puurunen, W. M. M. Kessels, and H. C. M. Knoops, J. Phys. Chem. C **123**, 27030 (2019).
- 14R. L. Puurunen, in *International Workshop Atomic Layer Deposition Russia 2015, ALD Russia 2015*, September 21–23, 2015, Moscow Institute of Physics and Technology, Dolgoprudny, Russia (Moscow Institute of Physics and Technology, Dolgoprudny, Russia, 2015).
- 15 J. Yim, O. M. E. Ylivaara, M. Ylilammi, V. Korpelainen, E. Haimi, E. Verkama, M. Utriainen, and R. L. Puurunen, Phys. Chem. Chem. Phys. 22, 23107 (2020)
- <sup>16</sup>E. Langereis, S. B. S. Heil, H. C. M. Knoops, W. Keuning, M. C. M. van de Sanden, and W. M. M. Kessels, J. Phys. D: Appl. Phys. 42, 073001 (2009).
- <sup>17</sup>E. Langereis, S. B. S. Heil, M. C. M. Van De Sanden, and W. M. M. Kessels, J. Appl. Phys. **100**, 023534 (2006).
- <sup>18</sup>E. A. Irene, In Situ Real-Time Characterization of Thin Films (Wiley, New York, 2001).
- <sup>19</sup>M. Hilfiker et al., Appl. Phys. Lett. **120**, 132105 (2022).
- <sup>20</sup>U. Kılıç, D. Sekora, A. Mock, R. Korlacki, S. Valloppilly, E. M. Echeverría, N. Ianno, E. Schubert, and M. Schubert, J. Appl. Phys. **124**, 115302 (2018).
- <sup>21</sup>D. Pal, J. Singhal, A. Mathur, A. Singh, S. Dutta, S. Zollner, and S. Chattopadhyay, Appl. Surf. Sci. 421, 341 (2017).
- <sup>22</sup>J. A. Spencer, A. L. Mock, A. G. Jacobs, M. Schubert, Y. Zhang, and M. J. Tadjer, Appl. Phys. Rev. 9, 011315 (2022).
- 23°C. Feit, S. Chugh, A. R. Dhamdhere, H. Y. Kim, S. Dabas, S. J. Rathi, N. Mukherjee, and P. Banerjee, J. Vac. Sci. Technol. A 38, 062404 (2020).
- <sup>24</sup>N. Kumagai, S. Yamasaki, and H. Okushi, Diamond Relat. Mater. **13**, 2092 (2004).
- 25 U. Kilic, A. Mock, D. Sekora et al., Sci. Rep. 10, 10392 (2020).
- <sup>26</sup>V. Cremers, F. Geenen, C. Detavernier, and J. Dendooven, J. Vac. Sci. Technol. A 35, 01B115 (2017).
- <sup>27</sup>R. G. Gordon, D. Hausmann, E. Kim, and J. Shepard, Chem. Vap. Deposition 9, 73 (2003).
- J. Dendooven, D. Deduytsche, J. Musschoot, R. L. Vanmeirhaeghe, and C. Detavernier, J. Electrochem. Soc. 156, P63 (2009).
- <sup>29</sup>M. K. Gobbert, V. Prasad, and T. S. Cale, Thin Solid Films **410**, 129 (2002).
- 30 A. V. Fadeev and K. V. Rudenko, Tech. Phys. 63, 1525 (2018).
- <sup>31</sup> M. Weismann, D. F. G. Gallagher, and N. C. Panoiu, J. Opt. 17, 125612 (2015).
- <sup>32</sup>M. G. Moharam and T. K. Gaylord, J. Opt. Soc. Am. A 3, 1780 (1986).
- 33 D. Gkogkou et al., Appl. Surf. Sci. 421, 460 (2017).
- 34M. G. Moharam and T. K. Gaylord, J. Opt. Soc. Am. 71, 811 (1981).
- 35M. G. Moharam and T. K. Gaylord, J. Opt. Soc. Am. 73, 1105 (1983).
- <sup>36</sup>M. G. Moharam, T. K. Gaylord, E. B. Grann, and D. A. Pommet, J. Opt. Soc. Am. A 12, 1068 (1995).
- <sup>37</sup>A. C. Diebold, A. Antonelli, and N. Keller, APL Mater. 6, 058201 (2018).
- <sup>38</sup>W.-N. Wang, F. Wu, Y. Myung, D. M. Niedzwiedzki, H. S. Im, J. Park, P. Banerjee, and P. Biswas, ACS Appl. Mater. Interfaces 7, 5685 (2015).
- <sup>39</sup>Y. C. Park, B. C. Park, S. Romankov, K. J. Park, J. H. Yoo, Y. B. Lee, and J.-M. Yang, J. Microsc. **255**, 180 (2014).
- 40 L. Fang, H. Li, X. Ma, Q. Song, and R. Chen, Appl. Surf. Sci. 527, 146818 (2020).
- <sup>41</sup>G. E. Jellison, F. A. Modine, P. Doshi, and A. Rohatgi, Thin Solid Films 313–314, 193 (1998).
- <sup>42</sup>G. E. Jellison, in *Handbook of Ellipsometry*, edited by H. G. Tompkins and E. A. Irene (William Andrew Publishing, Norwich, NY, 2005), pp. 237–296.
- <sup>43</sup>R. A. Zargar, K. Kumar, Z. M. M. Mahmoud, M. Shkir, and S. AlFaify, Physica B 631, 413614 (2022).
- 44H. Zheng et al., J. Phys. Chem. C 120, 22532 (2016).
- <sup>45</sup>S. Sharma, C. Periasamy, and P. Chakrabarti, Electron. Mater. Lett. 11, 1093
- <sup>46</sup>I. Perez, E. Robertson, P. Banerjee, L. Henn-Lecordier, S. J. Son, S. B. Lee, and G. W. Rubloff, Small 4, 1223 (2008).
- <sup>47</sup>See the supplementary material at https://www.scitation.org/doi/suppl/ 10.1116/6.0001937 for EMA.